

# Reactive deposition epitaxy of $\text{CoSi}_2$ nanostructures on $\text{Si}(001)$ : Nucleation and growth and evolution of dots during anneal

I. Goldfarb\* and G. A. D. Briggs

*Department of Materials, University of Oxford, Parks Road, Oxford OX1 3PH, United Kingdom*

(Received 4 January 1999; revised manuscript received 4 February 1999)

Nucleation dependence of reactively deposited  $\text{CoSi}_2/\text{Si}(001)$  morphology and structure were analyzed *in situ* by scanning tunneling microscopy and surface electron diffraction. On a flat surface, Volmer-Weber growth results in a mixture of faceted  $\text{CoSi}_2(221)-c(2\times\sqrt{3})-$  and flat-topped  $\text{CoSi}_2(001)-c(2\times 4)-$  reconstructed three-dimensional nanocrystals (dots). To test their stability, the dots were annealed at the growth temperature for prolonged periods of time. The initial dot shape was found to be metastable against elongation, as the mean size increased significantly with annealing time. However, eventually the dot arrays attained a state closer to equilibrium, as could be judged from the transition to a more laterally isotropic shape, simultaneously with a reduction of the mean dot size. This “inverse coarsening” is achieved by partial dissolution of the dots, with the excess material transferred onto the interdot silicon area, converting it into a silicide. Growth on a  $3^\circ$ -off vicinal surface results in two-dimensional  $p(2\times 2)+c(2\times 2)-$ reconstructed platelets. These observations may have important implications for the semiconductor industry. [S0163-1829(99)00231-3]

## I. INTRODUCTION

$\text{CoSi}_2$  is attractive as a self-aligned silicide for high-performance ultralarge scale integrated (ULSI) devices because of its low lattice mismatch with Si,  $\approx -1.2\%$ , and low electrical resistivity,  $\approx 14 \mu\Omega \text{ cm}$ .<sup>1,2</sup> However, epitaxial  $\text{CoSi}_2$  films of high structural quality have only been found to grow on  $\text{Si}(111)$  substrates, while growth on the more important  $\text{Si}(001)$  substrates results in misoriented grains.<sup>3,4</sup> Recent scanning tunneling microscopy (STM) observations of  $\text{CoSi}_2/\text{Si}(001)$  growth, by reactive deposition epitaxy (RDE) and molecular beam epitaxy (MBE), have revealed the formation of small three-dimensional (3D) islands of different geometrical shapes.<sup>5</sup> While smoother layers can be achieved with the aid of a so-called “template” technique,<sup>4,6,7</sup> the small size and apparent crystalline perfection of the 3D islands imply the fascinating possibility of using them as self-assembled metallic quantum dots. There is, however, an additional necessary requirement for the latter purpose, i.e., the uniformity of size and shape of the dots in the array, which is usually the most difficult part of the self-assembled dot growth.<sup>8-10</sup> Another fascinating possibility is to use the dots to detect an infrared radiation in an internal photoemission sensor device, where the quantum efficiency due to  $\text{CoSi}_2$  nanoparticles is six times higher than in planar  $\text{CoSi}_2$  Schottky diodes.<sup>11</sup> As the self-assembled dots in this study are obtained in a more straightforward fashion, and their degree of perfection and possibility of control appear to be better than in Ref. 11, even higher quantum efficiency seems viable.

Deeper understanding of  $\text{CoSi}_2/\text{Si}(001)$  growth may improve the quality of flat layers for ULSI applications or 3D nanocrystals for quantum dot devices, which has been the motivation for the present study. In particular, we aimed to explore the effects of the silicide terrace nucleation and step-edge nucleation on the resulting morphology, and to determine whether the structures obtained are kinetically limited

or in thermodynamic equilibrium. Indeed, we have found that cobalt silicide nucleation on terraces resulted in the appearance of nonequilibrium 3D nanocrystals on the surface, while nucleation at double-height step edges produced 2D platelets closer to equilibrium. By performing a detailed quantitative analysis of the nanocrystal late-stage growth kinetics, we have shown that even though initially metastable, they can be brought closer to equilibrium by prolonged anneals at elevated temperature. The late growth stages occur under the conditions of mass conservation, where the initial flux or supersaturation, which drives the nucleation, ceases to exist. These late stages have been frequently attributed to Ostwald ripening, which has been observed to take place in many materials systems.<sup>12</sup> However, various competing mechanisms, such as the static or dynamic coalescence,<sup>10,12</sup> strain, and different attachment-detachment barriers,<sup>9</sup> can make the interpretation ambiguous. For example, not only the late, but even the early stages of  $\text{Ge/Si}$  growth<sup>13</sup> have been attributed to Ostwald ripening by several groups,<sup>13-15</sup> while different mechanisms have been found to dominate by the others.<sup>9,10,16,17</sup> For the  $\text{CoSi}_2/\text{Si}(001)$  nanocrystals, we have found static coalescence to dominate the late growth stages, until transition from elongated to laterally isotropic shapes took place.

## II. EXPERIMENT

Therefore, two types of  $\text{Si}(001)$  wafer were chosen: flat, very slightly contaminated with Ni (below the detectability limit of our Auger analyzer); and clean  $3^\circ$ -off vicinal wafers. Narrow terraces of the latter were supposed to ensure sufficiently high probability of the adatoms to reach the step edges before nucleating an island, while wider terraces and Ni-induced trenches<sup>18</sup> of the former were supposed to restrict surface diffusion and to achieve the opposite effect. In UHV, the substrates were degassed for several hours and repeatedly flashed at 1400 K and a pressure  $\leq 10^{-7}$  Pa, before slow cooling to the desired temperature. Such treatment has gen-

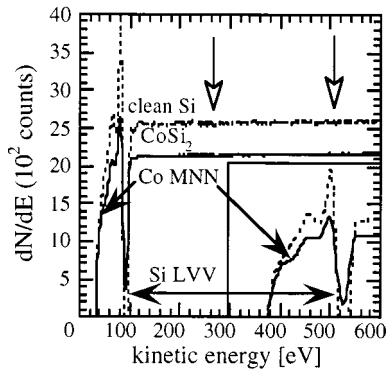


FIG. 1. 2 kV Auger spectra of the initial Si substrate (dotted line) and the  $\text{CoSi}_2/\text{Si}(001)$  grown on top of it, at the end of the experiment (solid line). Note the absence of elements other than Si and Co, e.g., C and O at the spectral locations indicated by open arrowheads, and the “pumping” of intensity from the Si LVV peak at 92 eV into Co MNN peak at 53 eV in the grown layer.

erally proved effective in producing well-ordered  $(1 \times 2)$  Si surfaces.<sup>19</sup> Indeed, for the clean vicinal sample, this treatment resulted in single-domain  $(1 \times 2)$  terraces separated by double-layer  $D_B$  steps.<sup>20</sup> For the Ni-contaminated flat sample, it resulted in a trenched  $(2 \times N)$  surface (where  $9a < N < 10a$ ,  $a = 3.84 \text{ \AA}$  being the Si surface lattice constant), as expected.<sup>18</sup> A JEOL elevated-temperature STM, equipped with reflection high energy electron diffraction (RHEED) and low energy electron diffraction (LEED)/Auger spectrometer, and capable of operation up to 1500 K was used. The base pressure of the STM chamber prior to growth was  $1 \times 10^{-8}$  Pa. The constant-current images were taken using electrochemically etched  $W$  tips, during exposure to a flux of Co atoms at 770 K growth temperature (achieved by direct current resistive heating and measured by infrared pyrometer with  $\pm 30$  K accuracy). Co was supplied from a water-cooled four-element  $e$ -beam source at  $45^\circ$  to the sample, and the pressure during evaporation did not exceed  $10^{-7}$  Pa. After the deposition the sample was left to anneal at the same temperature for prolonged periods of time, and STM images were periodically taken to evaluate the changes to the sample surface. It should be noted that, in spite of the long annealing times in this study, very low pressure in UHV combined with rather high sample temperature reduced the adsorption onto the surface to a negligible level. Even after a few days, the only species detected in our Auger spectra were Si and Co (see Fig. 1).

### III. DEPENDENCE OF THE EVOLVING MORPHOLOGY AND STRUCTURE ON THE SUBSTRATE CONFIGURATION AND NUCLEATION SITE

#### A. Terrace-nucleation on a flat Si(001) surface

Comparison of STM images in Fig. 2 to those in Fig. 3, and of the corresponding electron diffraction patterns in Fig. 4, indicates a marked difference in the silicide growth morphology on flat and vicinal substrates. In both cases, about 0.8 ML of Co was deposited, as estimated from the total volume of  $\text{CoSi}_2$  nanocrystals/unit area on the flat substrate.

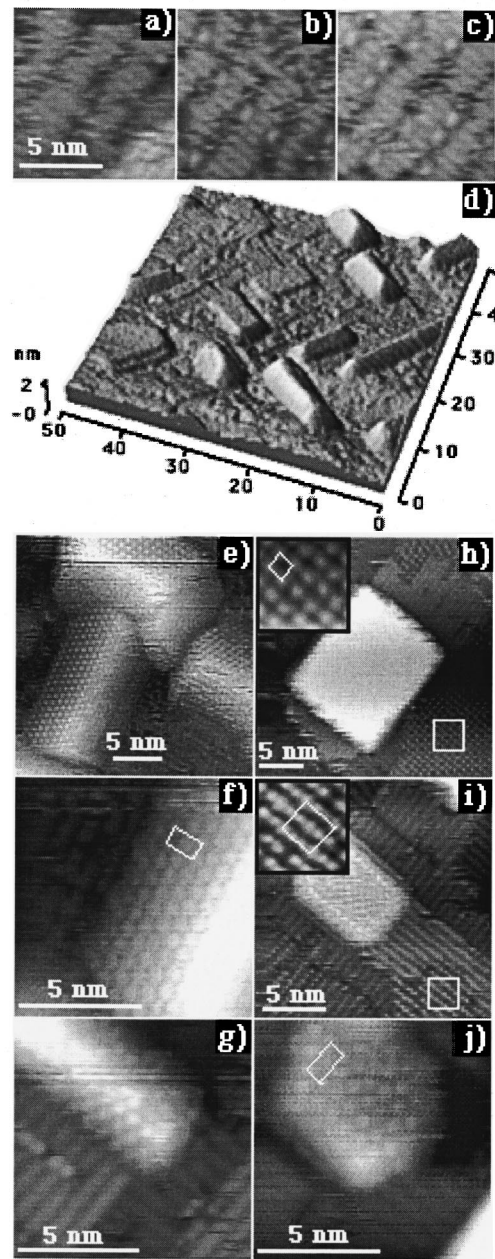


FIG. 2. STM images of (a)–(c): terrace nucleation; and (d)–(j): the resulting 3D morphology of cobalt silicide islands grown on a flat Si(001) surface. (a)–(c)–Constant-current images showing preferential island nucleation at the trenches ( $-1.5$  V,  $0.08$  nA). (d) 3D representation of the typical silicide islands (note the 3D flat-top islands and faceted huts oriented parallel to  $\langle 110 \rangle$  directions). (e)–(g) High-resolution images of the typical silicide huts, where the left-hand facet in (e) is blown up in (f) [(e), (f)  $+0.3$  V and  $0.1$  nA; (g)  $-0.5$  V and  $0.08$  nA]. (h)–(j) High-resolution images of the typical flat-top silicide islands ( $+0.5$  V and  $0.08$  nA,  $+0.3$  V and  $0.08$  nA, and  $-1$  V and  $0.08$  nA, respectively). Insets in (h) and (i) are blowups of the boxed regions at the bottom right.  $c(2 \times \sqrt{3})$ ,  $p(2 \times 2)$ ,  $c(4 \times 4)$ , and  $c(2 \times 4)$  unit cells are outlined in (f), (h), (i), and (j), respectively.

(Bearing in mind that some Co atoms may have gone into the interisland area, cf. IV B, the actual Co coverage could be slightly higher, but still less than a monolayer.) While in the former case the surface is composed of 3D nanocrystals [Fig.

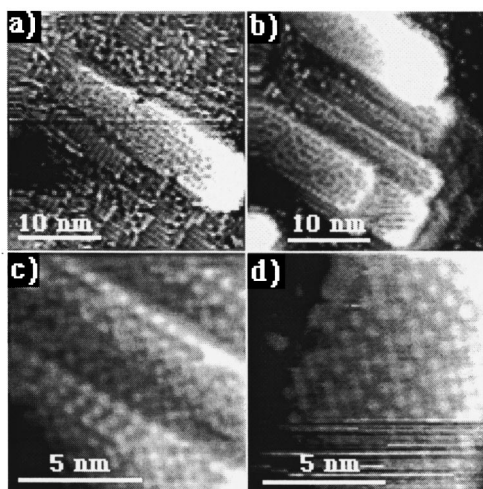


FIG. 3. Constant-current STM images of (a) step nucleation ( $-2$  V and  $0.08$  nA), and (b)–(c) the resulting 2D platelets of cobalt silicide grown on a  $3^\circ$ -off vicinal Si(001) surface ( $-1.5$  V and  $0.08$  nA).  $p(2 \times 2)$  and  $c(2 \times 2)$  unit cells are apparent in high-resolution images in (c) and, especially, in the upper-right corner of (d).

2(d)), of faceted [Figs. 2(e)–2(g)], or flat-topped [Figs. 2(h)–2(j)] shape, the latter consists of arrays of double-layer 2D platelets (Fig. 3). The 3D character of the nanocrystals, and 2D though multilevel character of the platelets, are well reflected in the transmission-type spots [Fig. 4(a)] vs intense streaking [Fig. 4(d)]<sup>21</sup> in their respective  $[110]$ -RHEED patterns [the beam directions are indexed relative to the Si(001) crystallographic directions, as in Fig. 5(a)].  $[100]$  patterns from the nanocrystals indicate  $\times 4$  surface periodicity, while the platelets seem to be  $\times 2$  reconstructed (quarter- and half-order reflections are marked by white arrows in Figs. 4(b) and 4(e), respectively). Due to its normal-incidence geometry, LEED is relatively insensitive to inclined and 3D surfaces, and thus the pattern obtained from the nanocrystals [Fig. 4(c)] does not show the  $\times 4$  periodicity (though the presence of 3D features can be inferred from a very high diffused background intensity). A pattern from the less rough platelet surface in Fig. 4(f) does show the  $(\frac{1}{2}; \frac{1}{2})$  spot [absent in Fig. 4(c), see black arrows], in addition to  $\{1;0\}$ - and  $\{\frac{1}{2};0\}$ -type spots.

Nucleation on the flat surface takes place in the missing-dimer trenches. Figs. 2(a)–2(c) show the progression of the silicide nucleation with Co exposure. As coverage increases, the formation of 3D islands is favored even at the expense of some additional surface energy, because of the elastic relaxation.<sup>22,23</sup> In equilibrium, isolated  $\text{CoSi}_2$  huts grow with a square base until they reach a critical size of almost 200 nm, after which they elongate to minimize their energy.<sup>24</sup> Our huts become elongated at much smaller sizes (7–8 nm), indicating that they are not in equilibrium; this may be due to hut-hut interactions, or some kind of facet-growth instability,<sup>25</sup> similar to that observed for Ge/Si(001) huts.<sup>9</sup> The latter instability seems particularly likely, as the nonfaceted islands do not show the same tendency to elongate. Although at first glance the flat tops and the hut facets appear to exhibit similar reconstruction, such an impression is misleading, because the former are parallel to the Si(001) surface, while the latter are inclined to it. Two hut-facet incli-

nation angles were measured from the slope of the STM images,  $\Theta_1 = 15.3 \pm 1^\circ$  and  $\Theta_2 = 18.9 \pm 1.4^\circ$ , with only  $\Theta_1$  facets, such as the ones in Figs. 2(e)–2(g), atomically resolved. The dimensions of the centered unit cell at the flat tops [outlined in Figs. 2(j) and 5(a)] are  $7.8 \text{ \AA} \times 15 \text{ \AA}$ . Within the experimental resolution limit, these are in excellent agreement with  $2a$  and  $4a$  interatomic distances, respectively, found on the (001) plane. On the other hand, the long side,  $12.8 \text{ \AA}$ , of the centered  $\Theta_1$ -facet cell,  $7.8 \text{ \AA} \times 12.8 \text{ \AA}$  [outlined in Figs. 2(f) and 5(b)], could not be expressed as  $na$  on the (001) plane, but close to the double interatomic distance in a  $\langle 112 \rangle$  direction on the  $\{111\}$  plane. This fact and the apparent threefold symmetry suggest  $\{111\}$  as a possible facet plane, in which case the nanocrystal orientation is such that the  $\{111\}$  planes form a  $15.3^\circ$  angle with its  $\{hkl\}$  plane parallel to Si(001).  $\{221\}$  orientation matches this requirement, with the long side of the centered  $\{111\}$ -facet cell  $12.8 \text{ \AA} / \cos(15.79^\circ) = 13.3 \text{ \AA}$ , i.e., exactly double interatomic distance in a  $[\bar{1}12]$  direction [see Fig. 5(b)]. Thus the  $\{111\}$ -facet periodicity is conveniently described as  $c(2 \times \sqrt{3})$ . Furthermore, now the  $\Theta_2$  facets can be identified within the measurement error as  $\{110\}$  planes. Summarizing, the flat-topped nanocrystals were identified as  $c(2 \times 4)$ -reconstructed [relative to Si(001)- $(1 \times 1)$  bulk termination] epitaxial  $\text{CoSi}_2(001)$  with the cubic axes parallel to those of silicon, and the orientation relations of the faceted  $c(2$

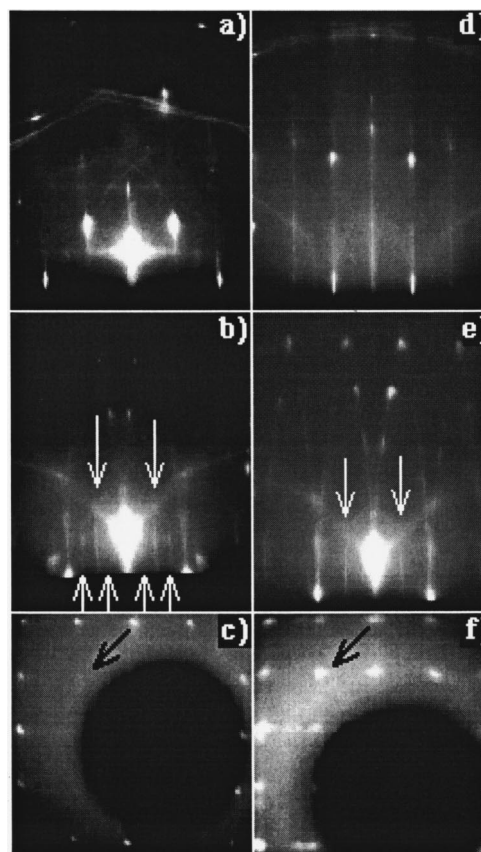


FIG. 4. (a), (b)  $[110]$  and  $[100]$  RHEED, and (c) LEED patterns from the 3D silicide surface, as in Fig. 2, and (d), (e)  $[110]$  and  $[100]$  RHEED, and (f) LEED patterns from the 2D platelet morphology, as in Fig. 3. Black (white) arrows in LEED (RHEED) point to fractional-order reflections.

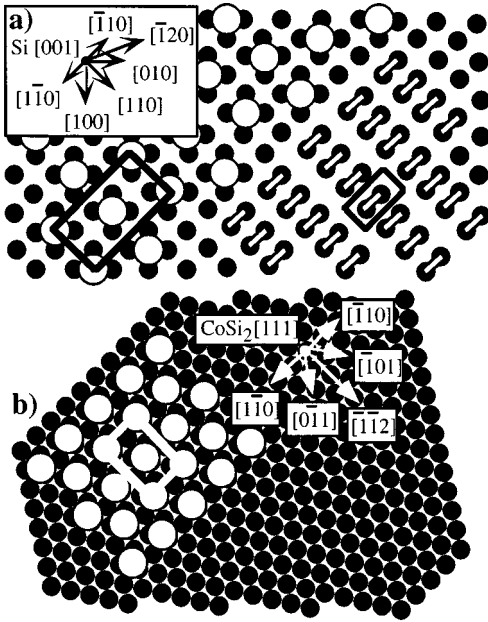


FIG. 5. Orientation relations of (a)  $\text{CoSi}_2(001)-c(2 \times 4)/\text{Si}(001)-(2 \times 1)$ , and (b)  $\text{CoSi}_2(221)-c(2 \times \sqrt{3})/\text{Si}(001)$  nanocrystals, as deduced, e.g., from Figs. 2(j) and 2(f), respectively.  $c(2 \times \sqrt{3})$  and  $p(2 \times 1)$ , and  $c(2 \times 4)$  unit cells are outlined in (a) and (b), respectively. Large empty circles represent the upper layer, small filled circles represent the second layer, and the bonded ones stand for dimers. Directions in a  $\text{Si}(001)$  plane are shown in the upper-left corner in (a), and directions in (111) facet of  $\text{CoSi}_2(221)$  crystal in (b). This schematic drawing should be regarded as purely geometrical, and does not provide the position and bonding configuration of the atoms.

$\times \sqrt{3}$ –reconstructed ones were determined to be  $\text{CoSi}_2(221)\|\text{Si}(001)$  and  $\text{CoSi}_2[\bar{1}10]\|\text{Si}[\bar{1}10]$  (see Fig. 5). Grains of the latter orientation have been observed by transmission electron microscopy (TEM),<sup>3,4</sup> forming  $\{001\}$ – $\{221\}$  and  $\{111\}$ – $\{111\}$ , or  $\{511\}$ – $\{111\}$  twin boundaries with the underlying silicon, with the interface Co atoms seven- or eightfold coordinated. The combination of high coordination and close lattice match over a wide temperature range lends stability to this orientation.<sup>3</sup>

### B. Step-edge nucleation on vicinal $\text{Si}(001)$ surface

A  $3^\circ$ -off vicinal  $\text{Si}(001)$  surface contains double-height  $D_B$  steps, separated by 5-nm-wide terraces [i.e.,  $0.27 \text{ nm}/\tan(3^\circ)$ ]. When Co is deposited onto this surface, 2D silicide platelets nucleate at the step edges, as can be seen in Fig. 3(a). As the growth continues further, the platelets mimic the configuration of the substrate by creating arrays of double-height silicide steps separated by approximately 5-nm-wide terraces [see Fig. 3(b)]. Such a growth is realized via silicide bilayers, where every bilayer can be regarded as an extension of the  $\text{Si } D_B$  step edge where it was nucleated. The observed morphology seemed to be unaffected by a prolonged anneal at the growth temperature. As  $\text{CoSi}_2$  is always terminated by at least one monolayer of Si, double-height steps are representative of a Si-rich  $S$  surface,<sup>26–28</sup> which is also confirmed by a characteristic mixture of  $c(2 \times 2)$  +  $p(2 \times 2)$  reconstructions at the platelet surface [see Fig.

3(d)].<sup>7</sup> The  $(3\sqrt{2} \times \sqrt{2})$ – $R45^\circ$  reconstruction of the  $S$  surface<sup>7</sup> was not observed by STM or RHEED and LEED in this study, although atomic shifts leading to this reconstruction could be recognized at the platelet edges [cf. Fig. 3(c)]. Since 3D  $\text{CoSi}_2$  island nucleation has been observed even at the  $\text{Si}(001)$   $S_B$  edges,<sup>5</sup> the stepped platelet morphology discussed above is not simply due to step-edge nucleation, but involves specific interaction of growing  $\text{CoSi}_2$  with  $D_B$  edges and single-domain  $(1 \times 2)$  terraces. In equilibrium, step-step separations,  $l$ , on a surface are determined by competing interactions between force multipoles causing strain relaxation at the step edges.<sup>29–31</sup> For example, the force-dipole interaction term,  $\lambda_d a^2 l^{-2}$ , arises mainly due to the rebonding of  $S_B$  and  $D_B$  steps on  $\text{Si}(001)$ . However, due to the differences in atomic configuration between these two steps, their force-dipole coefficients,  $\lambda_d$ , differ considerably.<sup>31</sup> Thus, while it may be energetically favorable to accommodate the tension from the  $\text{CoSi}_2/\text{Si}$  mismatch by growing platelets extending the  $D_B$  silicon steps, at the  $S_B$  step edges 3D islands may prove more effective in relaxing the tension. It is difficult to make a more quantitative analysis because the exact structure and force-multipole coefficients of the  $\text{CoSi}_2$  surface are not known. However, there are at least two important similarities with a vicinal  $\text{Si}(001)$  surface: (i) it contains descending double-height steps separated by single-domain terraces, and (ii) contrast enhancement at the edges [see Fig. 3(c)] can be attributed to rebonding.<sup>32</sup> It is therefore possible that the stepped platelet structure is stabilized by the force-dipole interaction between the steps and the force-monopole interaction due to mismatch strain. The latter monopole differs from the dimerization induced one,<sup>30,31,33</sup> and arises because the applied strain on one side of the step is not balanced by an equal and opposite strain on the other side.<sup>34–36</sup> Thus, the step-edge atoms are able to partially relax by shifting outwards (inwards) under bulk compression (tension). Since the sign of this monopole does not alternate for successive steps, it causes logarithmic attraction  $\lambda_e \ln(l)$  between them [where  $\lambda_e$  is proportional to  $(\text{strain} \times \text{step height})^2$  (Refs. 34 and 35)], which can ultimately lead to step bunching.<sup>35</sup> The equilibrium platelet width,  $l_0 = a \sqrt{(2\lambda_d/\lambda_e)}$ , is then obtained by minimizing the energy of the stepped array,  $\{\lambda_0 + \lambda_d a^2 l^{-2} + \lambda_e \ln(l)\}$ , with respect to  $l$  (where  $\lambda_0$  is the  $\text{CoSi}_2$  double-height step formation energy due to bond breaking, dangling bonds, and elastic deformation<sup>30</sup>). Knowing  $\lambda_d$ , one can determine whether the stepped arrays of 5-nm-wide platelets shown in Fig. 3 represent an equilibrium configuration. In general, however, the sign of strain should also be considered,<sup>34,37</sup> since it determines the sign of the monopole-dipole cross term.<sup>33,38</sup>

## IV. LATE-STAGE GROWTH OF $\text{CoSi}_2$ DOTS

### A. Kinetics of the nanocrystal island growth

The surface immediately after Co deposition is shown in Fig. 6(a), and consists of faceted  $\text{CoSi}_2(221)-c(2 \times \sqrt{3})$ – and flat-topped  $\text{CoSi}_2(001)-c(2 \times 4)$ –reconstructed three-dimensional nanocrystals, which coarsen with annealing time [Figs. 6(b)–6(c)]. The size distributions (SD's) corresponding to Figs. 6(a)–6(d) are shown in Figs. 7(a)–7(d), respectively. Continuous elongation of the distribution tail towards

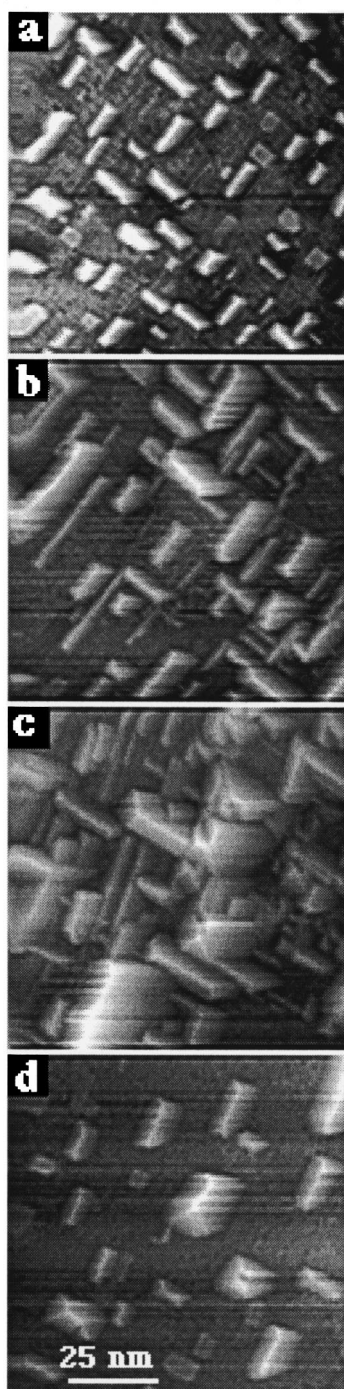


FIG. 6. Constant-current STM images showing the evolution of  $\text{CoSi}_2/\text{Si}(001)$  nanocrystals with annealing time. (a) 1 h ( $-2$  V and 0.08 nA), (b) 18 h ( $-5$  V and 0.08 nA), (c) 66 h ( $-5$  V and 0.08 nA), and (d) 111 h ( $-5$  V and 0.08 nA).

the large-size end, causing strong positive skewness, is immediately apparent when going from Fig. 7(a) to Fig. 7(c), and even more so in the nanocrystal volume distribution (VD) given in the insets. It is also apparent that Figs. 6(d) and 7(d) deviate from this trend. To guide the eye, the SD's and VD's were fitted with the normal Gaussian curves, as well as with the log-normal curves. While 1 h after the deposition both the SD and VD are rather symmetrical and well-fitted with the Gaussians, the positively skewed distributions at the later annealing times, with the exception of (d), are

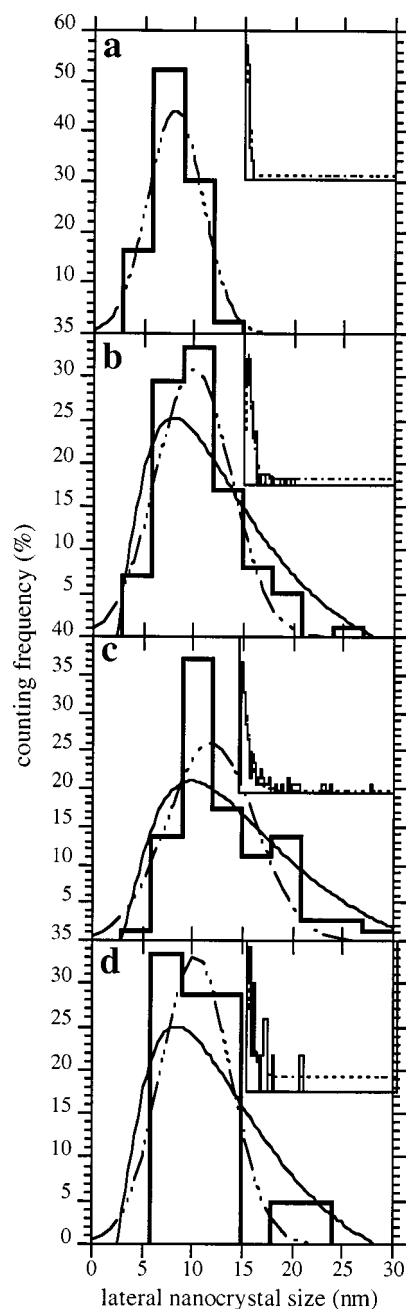


FIG. 7. Size and volume (inset) distributions of  $\text{CoSi}_2/\text{Si}(001)$  nanocrystals at various stages of anneal. (a) 1 h, (b) 18 h, (c) 66 h, and (d) 111 h. The best fits to normal (dashed-dotted lines) and log-normal (solid lines) distribution are presented.

best fitted with the log-normal curves. Existence of nanocrystals larger than twice the mean size is a clear fingerprint of coalescence. In the Ostwald ripening-type process the maximum particle size is restricted to  $2\langle r \rangle$  (or even less in the original formulation of Lifshitz and Slyozov<sup>39</sup>), where  $\langle r \rangle$  is the mean particle size in equilibrium with the surroundings, neither shrinking nor growing.<sup>12</sup> However, such restrictions are not imposed on the coalescing particles. When two such particles, which can be both larger than  $\langle r \rangle$ , encounter, fast diffusive interaction causes them to coalesce. The result is the removal of these particles from the smaller-size range of the SD, and adding an arbitrarily large particle to the

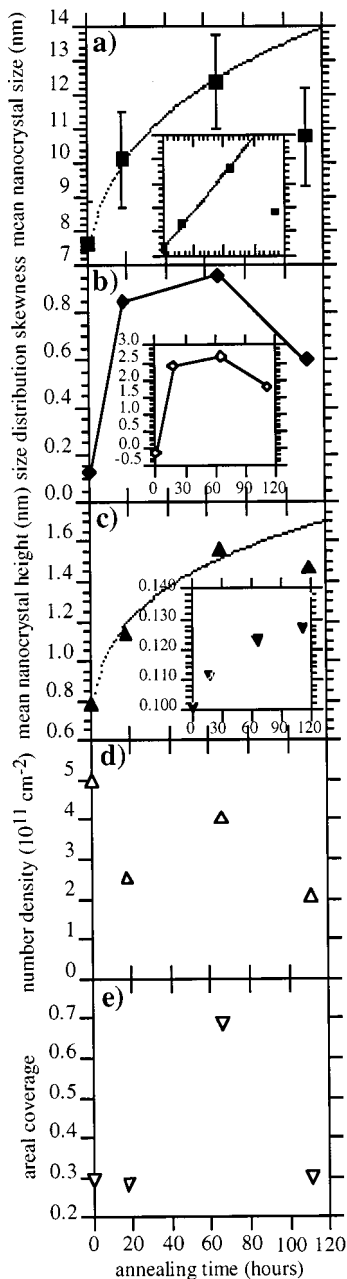


FIG. 8. Time dependence of (a) mean nanocrystal size fitted with  $r(t) = r_0[1 + k(t - t_0)]^{1/5}$  (dotted line), inset: linear fit to  $r^5(t) = r_0^5 + k(t - t_0)$ ; (b) size distribution skewness, inset: volume distribution skewness, where solid lines only guide the eye; (c) mean nanocrystal height fitted with  $h(t) = h_0[1 + k(t - t_0)]^{1/5}$  (dotted line), inset: vertical nanocrystal aspect ratio; (d) nanocrystal number density; and (e) fraction of the area covered by nanocrystals.

larger-size range, which explains the positive skewness and long large-size tail. Coalescing nanocrystals are clearly observed in Figs. 6(b) and 6(c).

To estimate the kinetics, we have plotted  $\langle r \rangle$  as a function of time in Fig. 8(a). (In view of the strongly skewed nature of the SD's and, especially, VD's, we have used the geometric mean and standard deviation, which better characterize log-normal-type distributions.) For the annealing time  $t \leq 66$  h the mean nanocrystal size and height [Figs. 8(a) and 8(c)], were found to obey power law of the form  $r(t)$ ,  $h(t)$

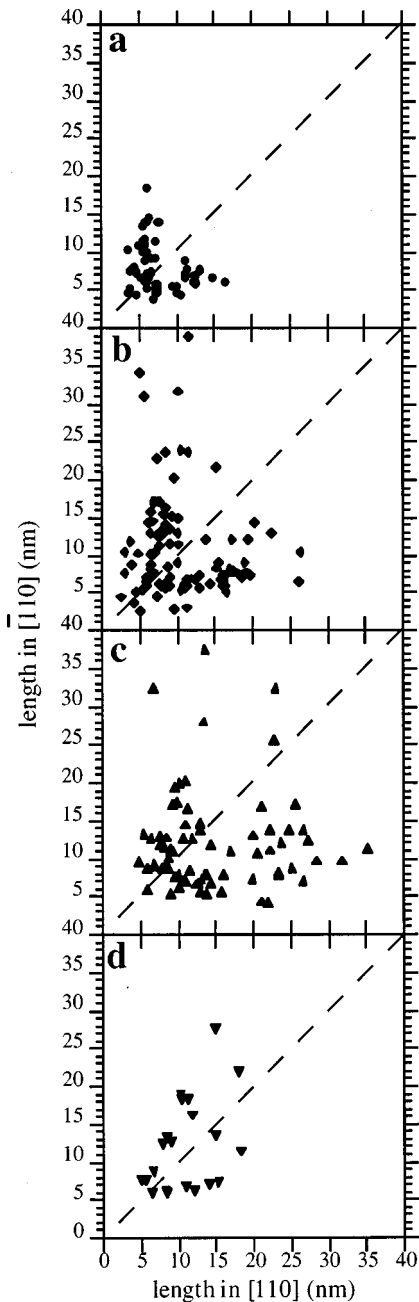


FIG. 9. Variation of the growth anisotropy of the nanocrystals with annealing time, expressed as the nanocrystal length in the  $[\bar{1}10]$  direction vs the length in  $[110]$  direction. Values close to a line at  $45^\circ$  intersecting the origin represent isotropic nanocrystals.

$= r_0, h_0[1 + k(t - t_0)]^{1/n}$ . [The SD and VD skewness were observed to follow the same trend: Fig. 8(b) demonstrates the droppage of the skewness values after 66 h of anneal.] The more reliable way of finding the exponent of a strongly nonlinear function, is by converting it to a linear one, and thus we have performed fits to a function of the type  $r^n(t) = r_0^n + k(t - t_0)$ . The best fit was obtained for  $n = 5$  [inset of Fig. 8(a)]. This is a striking result, as the same  $r \propto t^{1/5}$  dependence was found for the growth of Ge nanocrystals on Si(001) and attributed to a transport-limited growth.<sup>9</sup> This implies that, similarly to the growth of thicker  $\text{CoSi}_2$  films, the growth of  $\text{CoSi}_2$  nanocrystals is not controlled by the Si-Co reaction. However, while the parabolic dependence of

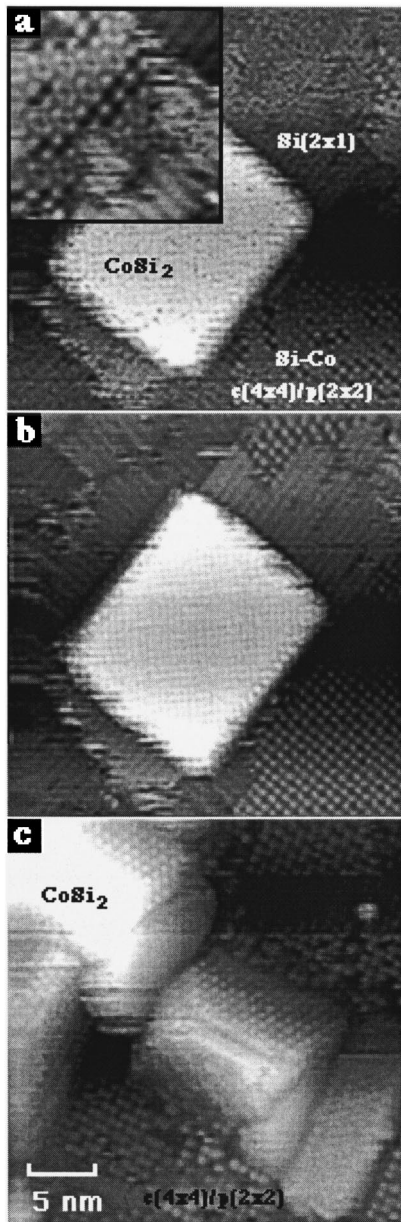


FIG. 10. Constant-current STM images showing the transition of  $\text{Si}(2 \times 1)$  interisland area into a mixture of Co-Si  $c(4 \times 4)$  and  $p(2 \times 2)$  phases (see text for details). (a) 18 h of anneal (+1.5 V and 0.08 nA); (b) same as in (a), but +0.5 V and 0.08 nA; (c) 66 h (-0.3 V and 0.08 nA). Inset in (a) is a blowup of the right-bottom region, demonstrating the mixed character of the  $c(4 \times 4)$  reconstruction.

the film thickness on time follows the trivial solution of Fick's diffusion equation,  $T = (Dt)^{1/2}$ ,<sup>1,40</sup> the  $t^{1/5}$  dependence indicates additional limitations to diffusion.<sup>9</sup> As will be shown below, one possible reason is that not all of the diffusing Co atoms (which are the main diffusants in the temperature range relevant to this experiment<sup>40</sup>) reach the nanocrystal islands; some of them are used to convert the interisland area into various Si-Co compounds.

Plotting the nanocrystal axial length along the  $[\bar{1}10]$  direction vs the length along the  $[110]$  direction, as shown in Fig. 9, helps to estimate the effect of anneal on the lateral growth anisotropy and provides another useful insight.<sup>17</sup> The

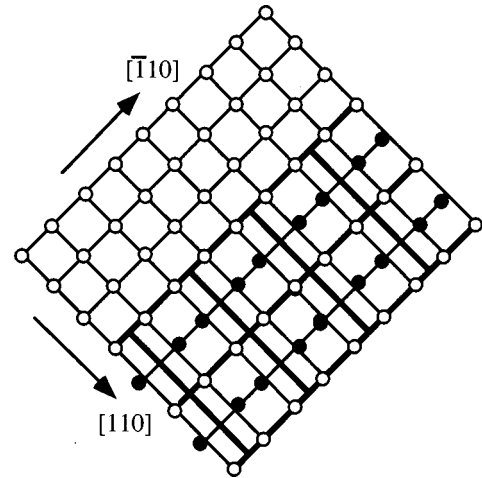


FIG. 11. Schematic drawing of the relation between  $p(2 \times 2)$  (thin lines) and  $c(4 \times 4)$  (thick lines) reconstructions.  $c(4 \times 4)$  can be obtained by shifting every second protrusion (filled circles) from their equilibrium positions in  $[110]$  rows of a  $p(2 \times 2)$  structure, in  $[\bar{1}10]$  and  $[1\bar{1}0]$  directions.

more isotropic the nanocrystals are, i.e., the more symmetric base they have, the closer they lie to a  $45^\circ$  line intersecting the origin. One can clearly see that the increase in the mean size, up to 66 h of anneal, is achieved by nanocrystal elongation in only one of the  $\langle 110 \rangle$  directions, indicated by the values scattered parallel to the plot axes. It seems likely that such growth is achieved by material addition to the nanocrystal facet, with corresponding elongation in a direction perpendicular to that facet, similar to that observed in Ge/Si(001).<sup>9,19,41</sup> However, after 111 h of anneal, a marked tendency towards a more isotropic shape is apparent in Fig. 6(d), as quantitatively displayed in Fig. 9(d).

### B. The interisland area

In a simple mass-conserved scenario, immediately after the termination of Co flux, the supersaturation that drives the nucleation of new nanocrystal islands is reduced, and most of the residual Co atoms diffusing on the surface (or subsurface<sup>42</sup>) join the existing islands. Therefore, as the islands grow and coalesce, as indeed follows from the positive skewness of the SD and VD in Fig. 7(b), their number density should decrease, in agreement with Fig. 8(d), up to 18 h of anneal. As the growth and coalescence continue, the fraction of the area covered by the islands should increase, while their number density decreases further. However, that is not what was experimentally observed. After 66 h of anneal, the SD and VD are even more skewed [see Fig. 7(c)], as expected from progressively coalescing nanocrystals, but both the island coverage and number density were increased [see Figs. 8(d) and 8(e)]. This can only happen if new islands are nucleated, which requires a new source of Co atoms. Furthermore, after 111 h of anneal, the mean island size, island coverage, and number density decreased, as shown in Fig. 8. These observations cannot be explained without allowing some material exchange with the interisland area.

Figure 10 shows typical  $\text{CoSi}_2$  nanocrystals and the surrounding interisland area under various bias conditions, after 18[(a)–(b)] and 66 [(c)] h of anneal. The structure and ori-

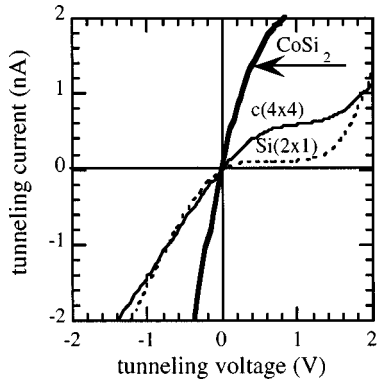


FIG. 12. Scanning tunneling spectra from  $(2 \times 1)$  (dotted line),  $c(4 \times 4)$  (thin line), and  $\text{CoSi}_2$  (thick line) regions. Note that the  $c(4 \times 4)$  spectrum is intermediate between the semiconducting  $(2 \times 1)$  spectrum and metallic  $\text{CoSi}_2$  one.

entation of these nanocrystals were discussed in Sec. III, so here we would like to focus on the interisland area. At the early annealing stages this area consists primarily of  $(2 \times 1)$ -reconstructed Si, and what seems to be  $c(4 \times 4)$ -reconstructed regions, and as the annealing progresses more and more  $(2 \times 1)$  regions are transformed into  $c(4 \times 4)$  regions [Figs. 10(a) and 10(b)]. This is a dynamic and reversible process. However, although we have occasionally observed a  $c(4 \times 4)$ -to- $(2 \times 1)$  transition, eventually all the  $(2 \times 1)$  regions are transformed into a  $c(4 \times 4)$ , as shown in Fig. 10(c). Close examination of voltage-dependent STM images revealed that this  $c(4 \times 4)$  reconstruction is actually a mixture of  $c(4 \times 4)$  and  $p(2 \times 2)$  [see Figs. 10(a) and 10(b)]. In fact, these two reconstructions are closely related, and Fig. 11 shows how the  $c(4 \times 4)$  structure can be obtained from a  $p(2 \times 2)$ , by periodic shifts. Although the exact nature of the bright protrusions forming the  $(2 \times 2)$  mesh is not yet known and even controversial,<sup>7,26,43</sup> this reconstruction, as well as  $c(4 \times 4)$ ,<sup>27,28</sup> has been observed and associated with Co-silicide surfaces by several authors.<sup>7,26–28,43</sup> Scanning tunneling spectra (STS) shown in Fig. 12 indicate that the electronic structure of such  $c(4 \times 4)$  differs from that of a clean silicon, as well as from that of a disilicide. Although more systematic STS studies are required, the nature of the  $I$ - $V$  curve from a  $c(4 \times 4)/p(2 \times 2)$  mixture, i.e., intermediate between semiconducting and metallic behavior, implies some sort of a Co-containing phase. As the solubility of Co in Si is negligible,<sup>1</sup> we attribute it to the formation of a silicide, perhaps poorer in Si than the disilicide.

### C. Towards the equilibrium

We therefore propose the following explanation of our observations. Some of the residual Co atoms, diffusing between the nanocrystal islands during the anneal, transform the initial  $\text{Si}(2 \times 1)$  interisland area into Co-Si compounds. These compounds serve as a reservoir in *local* quasiequilibrium with the islands, and thus material can be reversibly exchanged between them. This can explain the increase in island density after 66 h of anneal, if the supersaturation of Co contained in the reservoir is sufficient to drive the secondary nucleation of new islands (the primary nucleation has

vanished in the first 18 h of anneal, when there was no more free Co left). However, after 111 h of anneal, the epilayer was closer to a true equilibrium, which required far more isotropic island shapes.<sup>22,23</sup>

In the model proposed by Tersoff and Tromp,<sup>23</sup> the balance between the elastic relaxation of mismatch strain by the island and the additional surface energy of the island walls, causes such an island to have a square base in equilibrium. However, under the assumption of constant island height, when such an island reaches a certain critical size, elongation is favored to maintain a low mismatch strain, at least along one of the island axes. Using a special growth technique, based on implantation, Brongersma and coworkers have obtained unusually large and well-separated  $\text{CoSi}_2/\text{Si}(001)$  nanocrystal islands, and, by preventing secondary nucleation and island-island interaction effects, proved the validity of the model.<sup>24</sup> However, this model is not applicable to our experimental conditions for the following reasons: (i) our nanocrystal islands are smaller by at least one order of magnitude; (ii) they are closely spaced and island-island interaction cannot be neglected; (iii) secondary nucleation takes place; and finally, (iv) Fig. 8(c) shows that the island height varies almost by the factor of 2 during growth. Therefore the equilibrium model by Tersoff and Tromp<sup>23</sup> is not likely to account for the anisotropic island elongation shown here, which commences immediately and at island sizes significantly smaller than the critical 185-nm size found in Ref. 24. Furthermore, if the island height is allowed to vary, as in our case, square-based pyramids represent an equilibrium shape at *any* size.<sup>22</sup> Thus, the island elongation in our experiment is more likely to be explained by kinetic instability due to facet growth, as has been proposed by Jesson, Chen, and Pennycook for  $\text{Si}_x\text{Ge}_{1-x}/\text{Si}(001)$ ,<sup>25</sup> and experimentally confirmed by Goldfarb and coworkers.<sup>9,19,41</sup>

Elongated islands, such as the ones shown in Figs. 6(b)–6(c), can only transform into the more symmetrical ones, such as in Fig. 6(d), by detachment and outdiffusion of some of the island material. Since this material must go somewhere, e.g., into the interisland area, as the ‘‘equilibration’’ progresses one would expect to see more  $\text{Si}(2 \times 1)$  interisland area converted into a silicide, which is precisely what we observed. Figure 10(c) shows that even after 66 h of anneal there are practically no  $\text{Si}(2 \times 1)$  patches left, and after 111 h of anneal the islands are only slightly elongated [see Fig. 6(d)] and all the interisland area is  $c(4 \times 4)/p(2 \times 2)$  reconstructed. This island shape, rather than ideally square based, was proposed to be the equilibrium shape of a  $\text{CoSi}_2$  nanocrystal, with faceted rather than flat nanocrystal-substrate interfaces.<sup>44</sup> Thus, slightly elongated 3D silicide islands interconnected by a 2D silicide layer seem to represent a close to *global* equilibrium configuration. It is also worthy to note that, unlike all the parameters analyzed in Fig. 8, the vertical nanocrystal aspect ratio does not decrease even after 111 h of anneal [see inset of Fig. 8(c)]. Such an increase in aspect ratio can be expected, as by that time the nanocrystal size has increased by about 60% [Fig. 8(a)], and its volume by 300% (not shown), favoring steeper islands.<sup>22</sup> Finally, the (001)-oriented nanocrystals appear to be more stable than the (221)-oriented ones, as their respective ratio increases with annealing time [e.g., compare Fig. 6(a) to 6(d)].

## V. CONCLUSIONS

In conclusion, by changing the Si(001) substrate from a flat to a vicinal one during reactive deposition epitaxy of  $\text{CoSi}_2$ , we observed transition from 3D nanocrystal growth, which can be useful for self-assembled quantum-dot applications, to 2D platelet growth important for metallization in ULSI technology. These morphological differences can be linked to different nucleation sites on flat (terrace nucleation) and vicinal (step-edge nucleation) surface. [The importance of steps on vicinal Si(001) in promoting epitaxial silicide orientations has also been noted by Kennou *et al.*<sup>45</sup> based on their LEED analysis of  $\text{FeSi}_2$ .] To achieve a clear distinction between these two ultimate nucleation modes, we have used nominally flat and trenched, as well as single-domain vicinal Si(001) substrates. The trenches helped to avoid the otherwise inevitable mixed nucleation mode.<sup>5</sup> However, as similarly oriented nanocrystals have been observed by other groups<sup>3-6,24</sup> on nontrenched Si(001) substrates, we believe the trenches did not have any other major effect.

We have also studied the evolution of  $\text{CoSi}_2$  nanocrystal islands with annealing time at 770 K. This was achieved by monitoring the changes of various statistical parameters of the nanocrystal array at different stages of the anneal, primarily by *in situ* scanning tunneling microscopy. The nanocrystal growth was found to obey a power law, with the time exponent around 1/5, and was highly anisotropic with the elongation along only one of the  $\langle 110 \rangle$  nanocrystal axes. It continued to impingement with the neighboring nanocrystals, upon which diffusive interaction caused them to coalesce,

skewing the size and volume distribution functions to progressively positive values. The elongation did not match the equilibrium model, but rather implied a kinetic instability reflecting unequal probability of growth along different size facets, as was found for the Ge/Si(001) hut clusters. Because the  $\frac{1}{5}$  growth exponent was also identical to the one found in Ge/Si(001) huts, it indicated the  $\text{CoSi}_2$ /Si(001) nanocrystal growth was not controlled by the Co-Si reaction.

It was also found that the interisland area serves as a two-way reservoir, and plays an important role in establishing equilibrium. While initially the kinetics drives the anisotropic nanocrystal island elongation, after prolonged annealing times the thermodynamic tendency is to attain a more symmetric shape, which is achieved by outdiffusion from the islands into the interisland area. As a result, a transition to a more energetically favorable island shape takes place. Simultaneously, transformation of the  $\text{Si}(2 \times 1)$  interisland area into a  $c(4 \times 4)/p(2 \times 2)$  silicide mixture takes place, upon accommodation of the excess material from the islands.

The resulting configuration of still small, defect-free, and only slightly elongated disilicide nanocrystals, seemingly in equilibrium with the surrounding flat silicide layer, provides hope that they can be used as self-assembled metallic dots. Such dots can be used to improve the quantum efficiency of the internal photoemission sensors.

## ACKNOWLEDGMENT

The authors are grateful to J. Tersoff for useful discussions.

\*Electronic address: ilan.goldfarb@materials.ox.ac.uk; URL: <http://users.ox.ac.uk/~goldfarb/>

<sup>1</sup>S. P. Murarka, *Silicides for VLSI Applications* (Academic Press, New York, 1983).

<sup>2</sup>R. T. Tung and K. Inoue, in *Microscopy of Semiconducting Materials*, edited by A. G. Cullis and J. L. Hutchison, Institute of Physics Conference Series, Vol. 157 (Institute of Physics, London, 1997), p. 487.

<sup>3</sup>C. W. T. Bulle-Lieuwma, A. H. van Ommen, J. Hornstra, and C. N. A. Aussems, *J. Appl. Phys.* **71**, 2211 (1992).

<sup>4</sup>D. P. Adams, S. M. Yalisove, and D. J. Eaglesham, *J. Appl. Phys.* **76**, 5190 (1994).

<sup>5</sup>V. Scheuch, B. Voigtländer, and H. P. Bonzel, *Surf. Sci.* **372**, 71 (1997).

<sup>6</sup>V. Buschmann, M. Rodewald, H. Fuess, G. van Tendeloo, and C. Schäffer, *J. Cryst. Growth* **191**, 430 (1998).

<sup>7</sup>R. Stalder, C. Schwarz, H. Siringhaus, and H. von Känel, *Surf. Sci.* **271**, 355 (1992).

<sup>8</sup>F. Liu and M. G. Lagally, *Surf. Sci.* **386**, 169 (1997).

<sup>9</sup>I. Goldfarb, P. T. Hayden, J. H. G. Owen, and G. A. D. Briggs, *Phys. Rev. B* **56**, 10 459 (1997).

<sup>10</sup>Vinh Le Thanh, P. Boucaud, D. Débarre, Y. Zheng, D. Bouchier, and J.-M. Lourtioz, *Phys. Rev. B* **58**, 13 115 (1998).

<sup>11</sup>R. W. Fathauer, J. M. Iannelly, C. W. Nieh, and S. Hashimoto, *Appl. Phys. Lett.* **57**, 1419 (1990).

<sup>12</sup>M. Zinke-Allmang, L. C. Feldman, and M. H. Grabow, *Surf. Sci. Rep.* **16**, 377 (1992).

<sup>13</sup>F. M. Ross, J. Tersoff, and R. M. Tromp, *Phys. Rev. Lett.* **80**, 984 (1998).

<sup>14</sup>M. Zinke-Allmang, L. C. Feldman, S. Nakahara, and B. A. Davidson, *Phys. Rev. B* **39**, 7848 (1989).

<sup>15</sup>P. W. Deelman, T. Thundat, and L. J. Schowalter, *Appl. Surf. Sci.* **104/105**, 510 (1996).

<sup>16</sup>G. Medeiros-Ribeiro, A. M. Bratkovski, T. I. Kamins, D. A. A. Ohlberg, and R. S. Williams, *Science* **279**, 353 (1998).

<sup>17</sup>G. Medeiros-Ribeiro, T. I. Kamins, D. A. A. Ohlberg, and R. S. Williams, *Phys. Rev. B* **58**, 3533 (1998).

<sup>18</sup>H. Niehus, U. K. Kohler, M. Copel, and J. E. Demuth, *J. Microsc.* **152**, 735 (1988).

<sup>19</sup>I. Goldfarb, P. T. Hayden, J. H. G. Owen, and G. A. D. Briggs, *Phys. Rev. Lett.* **78**, 3959 (1997).

<sup>20</sup>D. J. Chadi, *Phys. Rev. Lett.* **59**, 1691 (1987).

<sup>21</sup>I. Goldfarb and G. A. D. Briggs, *Surf. Sci.* (to be published).

<sup>22</sup>J. Tersoff and F. K. LeGoues, *Phys. Rev. Lett.* **72**, 3570 (1994).

<sup>23</sup>J. Tersoff and R. M. Tromp, *Phys. Rev. Lett.* **70**, 2782 (1993).

<sup>24</sup>S. H. Brongersma, M. R. Castell, D. D. Perovic, and M. Zinke-Allmang, *Phys. Rev. Lett.* **80**, 3795 (1998).

<sup>25</sup>D. E. Jesson, K. M. Chen, and S. J. Pennycook, *MRS Bull.* **21**, 31 (1996).

<sup>26</sup>D. D. Chambliss, T. N. Rhodin, and J. E. Rowe, *Phys. Rev. B* **45**, 1193 (1992).

<sup>27</sup>G. Rangelov, P. Augustin, J. Stober, and Th. Fauster, *Phys. Rev. B* **49**, 7535 (1994).

<sup>28</sup>U. Starke, W. Weiss, G. Rangelov, Th. Fauster, G. R. Castro, and K. Henz, *Surf. Sci.* **352-354**, 89 (1996).

<sup>29</sup>V. I. Marchenko and A. Ya. Parshin, *Zh. Eksp. Teor. Fiz.* **79**, 257 (1980) [*Sov. Phys. JETP* **52**, 129 (1980)].

<sup>30</sup>O. L. Alerhand, D. Vanderbilt, R. D. Meade, and J. D. Joannopoulos, *Phys. Rev. Lett.* **61**, 1973 (1988).

- <sup>31</sup>T. W. Poon, S. Yip, P. S. Ho, and F. F. Abraham, *Phys. Rev. Lett.* **65**, 2161 (1990).
- <sup>32</sup>T. Komura, T. Yao, and M. Yoshimura, *Phys. Rev. B* **56**, 3579 (1997).
- <sup>33</sup>E. Pehlke and J. Tersoff, *Phys. Rev. Lett.* **67**, 465 (1991).
- <sup>34</sup>J. Tersoff, *Phys. Rev. Lett.* **74**, 4962 (1995).
- <sup>35</sup>J. Tersoff, Y. H. Phang, Z. Y. Zhang, and M. G. Lagally, *Phys. Rev. Lett.* **75**, 2730 (1995).
- <sup>36</sup>J. Tersoff, *Phys. Rev. Lett.* **80**, 2018 (1998).
- <sup>37</sup>Y. H. Xie, G. H. Gilmer, C. Roland, P. J. Silverman, S. K. Buratto, J. Y. Cheng, E. A. Fitzgerald, A. R. Kortan, S. Schuppler, M. A. Marcus, and P. H. Citrin, *Phys. Rev. Lett.* **73**, 3006 (1994).
- <sup>38</sup>J. Tersoff (private communication).
- <sup>39</sup>I. M. Lifshitz and V. V. Slyozov, *J. Phys. Chem. Solids* **19**, 35 (1961).
- <sup>40</sup>K. Maex, *Mater. Sci. Eng., R.* **11**, 53 (1993).
- <sup>41</sup>I. Goldfarb, J. H. G. Owen, D. R. Bowler, C. M. Goringe, P. T. Hayden, K. Miki, D. G. Pettifor, and G. A. D. Briggs, *J. Vac. Sci. Technol. A* **16**, 1938 (1998).
- <sup>42</sup>M. M. Y. Lee and P. A. Bennett, *Phys. Rev. Lett.* **75**, 4460 (1995).
- <sup>43</sup>H. Ikegami, H. Ikeda, S. Zaima, and Y. Yasuda, *Appl. Surf. Sci.* **117/118**, 275 (1997).
- <sup>44</sup>S. H. Brongersma, M. R. Castell, D. D. Perovic, and M. Zinke-Allmang, *J. Vac. Sci. Technol. B* **16**, 2188 (1998).
- <sup>45</sup>S. Kennou, N. Cherief, R. C. Cinti, and T. A. N. Tan, *Surf. Sci.* **211/212**, 685 (1989).